



# Cadomian (~560 Ma) crust buried beneath the northern Arabian Peninsula: Mineral, chemical, geochronological, and isotopic constraints from NE Jordan xenoliths



Robert J. Stern<sup>a,\*</sup>, Kamal A. Ali<sup>b</sup>, Minghua Ren<sup>c</sup>, Ghaleb H. Jarrar<sup>d</sup>, Rolf L. Romer<sup>e</sup>, Matthew I. Leybourne<sup>f</sup>, Martin J. Whitehouse<sup>g</sup>, Khalil M. Ibrahim<sup>h</sup>

<sup>a</sup> Geosciences Dept., U Texas at Dallas, Richardson, TX 75083-0688, USA

<sup>b</sup> Faculty of Earth Sciences, King Abdulaziz University, Jeddah, Saudi Arabia

<sup>c</sup> Dept. Geosciences, University of Nevada, Las Vegas, Las Vegas, NV 89154-4010, USA

<sup>d</sup> Department of Geology, The University of Jordan, P.O. Box 13633, 11942 Amman, Jordan

<sup>e</sup> GFZ German Research Centre for Geosciences, Potsdam, D-14473, Germany

<sup>f</sup> Department of Earth Sciences and Mineral Exploration Research Centre, Laurentian University, Sudbury, ON P3E 2C6, Canada

<sup>g</sup> Department of Geosciences, Swedish Museum of Natural History, Stockholm, SE-104 05, Sweden

<sup>h</sup> Department of Earth Sciences and Environment, The Hashemite University, Zarqa, Jordan

## ARTICLE INFO

### Article history:

Received 11 August 2015

Received in revised form 14 December 2015

Accepted 20 December 2015

Available online xxxx

Editor: A. Yin

### Keywords:

Cadomian

lower continental crust

Arabia

Jordan

xenolith

## ABSTRACT

In order to better understand the nature and formation of the lower continental crust beneath northern Arabia, we studied lower crustal xenoliths brought up by Neogene basalts in NE Jordan. Most of these xenoliths are comprised of primary phases plagioclase + two-pyroxenes with magnetite and ilmenite. Most clinopyroxene are augite whereas orthopyroxene mostly are hypersthene (Mg# = 50–80). Plagioclase feldspar is dominantly andesine–labradorite; pyrope-rich garnet and Fe-rich olivine (Fo<sub>75</sub> to Fo<sub>62</sub>) are rare. These xenoliths represent cumulates formed from intermediate magmas that pooled in the lower crust. Many xenoliths also contain small, fine-grained K-rich zones interpreted as melt pockets reflecting late magmatic infiltration of the lower crust. The xenoliths display a wide range in major element compositions (37–51 wt.% SiO<sub>2</sub>, 4–15 wt.% MgO and 0.1–6.3 wt.% TiO<sub>2</sub>), enrichment in Ba, K, Sr, Pb and Eu, and some trace element ratios atypical of bulk continental crust (e.g., K/Rb = 1265 ± 565, K/U = 63 000 ± 60 080 and Th/U = 0.96 ± 0.56); these extreme ratios reflect widespread K-metasomatism associated with melt pockets. The magmas from which these cumulates formed may have been generated at a reararc convergent margin setting. Four U–Pb zircon populations yield indistinguishable ages of 554 ± 4 Ma; 559 ± 5 Ma; 559 ± 6 Ma, and 563 ± 5 Ma. Initial <sup>87</sup>Sr/<sup>86</sup>Sr values (0.70260–0.70352) and positive εNd<sub>(560)</sub> (with the exception of a single, more radiogenic sample (+9.6), range = +1.3 to +4.8) indicate that the lower crust sampled by the xenoliths originated in the asthenospheric mantle, with little or no interaction with older crust, although Pb isotopic compositions allow for some interaction with older or subducted crustal materials. We interpret the geochemistry and mineralogy of these xenoliths to indicate that the lower crust beneath NE Jordan is mafic and comprised of plagioclase-rich 2-pyroxene igneous rocks. The lower crust of this area formed by magmatic underplating over less than 18 Ma. The crust of NE Jordan is significantly younger than the crust of the northernmost Arabian–Nubian Shield and represents a fragment of Cadomian (600–520 Ma) crust that may make up the NE margin of the Arabian Plate.

© 2015 Elsevier B.V. All rights reserved.

## 1. Introduction

Continental crust of the Arabian Plate provides a unique opportunity to study how juvenile continental crust forms, differentiates, and stabilizes. This crust is well-exposed in the Arabian Shield, the eastern half of the composite Arabian–Nubian Shield (ANS), and has been extensively studied, for both academic and economic pur-

\* Corresponding author.

E-mail addresses: [alik6588@yahoo.com](mailto:alik6588@yahoo.com) (K.A. Ali), [minghua.ren@unlv.edu](mailto:minghua.ren@unlv.edu) (M. Ren), [jarrargh@ju.edu.jo](mailto:jarrargh@ju.edu.jo) (G.H. Jarrar), [romer@gfz-potsdam.de](mailto:romer@gfz-potsdam.de) (R.L. Romer), [mleybourne@laurentian.ca](mailto:mleybourne@laurentian.ca) (M.I. Leybourne), [martin.whitehouse@nrm.se](mailto:martin.whitehouse@nrm.se) (M.J. Whitehouse), [ibrahim@hu.edu.jo](mailto:ibrahim@hu.edu.jo) (K.M. Ibrahim).

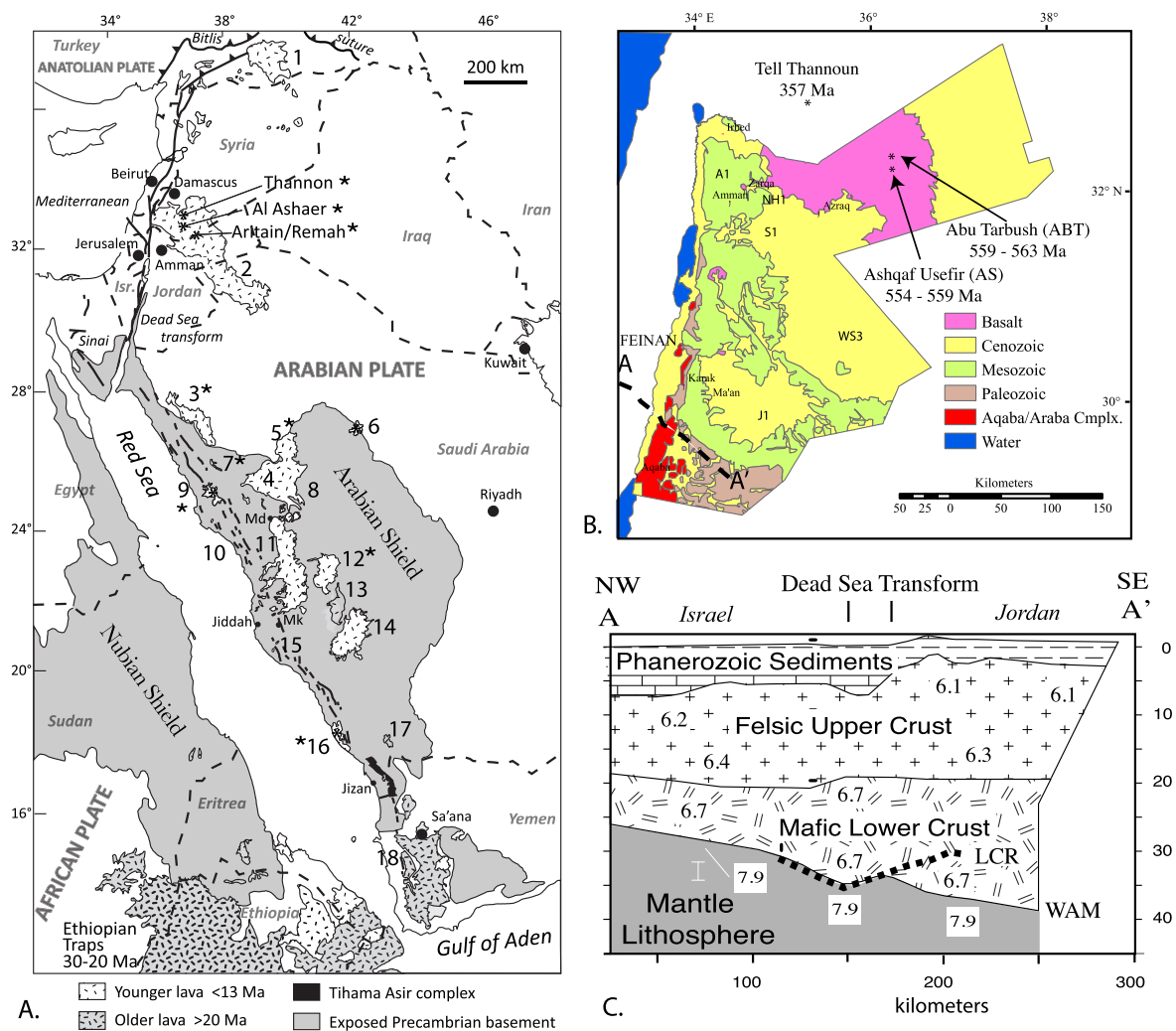


**Fig. 1.** A) Map of Cenozoic volcanic fields (harrats) of the western Arabian Plate and Neoproterozoic basement exposures of the Arabian–Nubian Shield (modified after Stern and Johnson, 2010). Locations of study sites Al Ashaer and Atrtain/Remah along with nearby Tell Thannoun (Stern et al., 2014) are shown. Young volcanic fields (harrats) are numbered: 1 = Karacalidag; 2 = Harrat Shaam; 3 = Harrat Uwayrid; 4 = Harrat Kura; 5 = Harrat Ithnayn; 6 = Harrat Hutaymah; 7 = Harrat Harairah; 8 = Harrat Khaybar; 9 = Harrat Lunayyir; 10 = mafic dikes (17–26 Ma); 11 = Harrat Rahat; 12 = Harrat Kishb; 13 = Harrat Hadn; 14 = Harrat Nawasif/Al Buqum; 15 = Harat Ad Damm; 16 = Harrat Al Birk; 17 = Harrat As Sirat; 18 = Yemen Traps with locations where lower crustal xenoliths have been studied are marked with \*. B) Simplified geologic map of Jordan, dashed line shows location of DESERT geophysical profile (Mohsen et al., 2006). Also shown are locations of wells penetrating Araba or Aqaba complex rocks comprising Neoproterozoic basement: A1 = Ajlun-1, NH1 = North Highlands-1; S1 = Safra-1; WS3 = Wadi Sirhan 3; J1 = Jafr-1 (Powell et al., 2015). C) 2-D P-wave velocity model (velocities in  $\text{km s}^{-1}$ ) across Jordan and Israel (profile A–A'; DESERT-Group, 2004). The thick dashed line near the Moho indicates the location of bands of strong reflections (LCR = Lower crustal reflectors; WAM–Moho inferred from wide-angle seismic profiling).

poses. Geochronologic and radiogenic isotope studies demonstrate that the Arabian Shield is mostly a juvenile composite magmatic addition from the mantle that was generated over  $\sim 300$  Ma in the Neoproterozoic Era (Stoeser and Frost, 2006; Robinson et al., 2015). From  $\sim 880$  until  $\sim 630$  Ma, juvenile crust formed at several intra-oceanic convergent margins (Hargrove et al., 2006), and these arc terranes coalesced along ophiolite-decorated sutures (Abdelsalam and Stern, 1997). Beginning about 630 Ma, the orogen evolved from Cryogenian accretionary tectonics to Ediacaran escape tectonics, characterized by the strike-slip Najd shear system (Meyer et al., 2014), lithospheric delamination (Avigad and Gvirtzman, 2009), and intense intraplate magmatism (Robinson et al., 2015). Crust of the northern part of the Arabian Plate is buried beneath thick sediments but we do not know if it is like that of the ANS or different.

Here we report results from integrated petrologic, geochemical, isotopic, and geochronological studies of gabbro, gabbro-norite, norite, and garnet clinopyroxenite from two volcanoes in NE Jordan,

Abu Tarbush and Ashqaf Usefir (Fig. 1A, B). We have two principal motivations for our study. First, we want to understand the origin of lower continental crust in general and the lower crust of Arabia in particular. Continental crust is typically  $\sim 40$  km thick and it is often stratified into felsic upper crust ( $V_p \sim 6.2$  km/s), amphibolitic middle crust ( $\sim 15$ – $25$  km deep;  $V_p \sim 6.2$ – $6.5$  km/s,  $\sim 60\%$   $\text{SiO}_2$ ), and mafic, granulitic lower crust ( $\sim 25$ – $40$  km deep;  $V_p \sim 6.8$ – $7.4$  km/s; ((Mooney et al., 1998; Rudnick and Gao, 2003) updated on <http://earthquake.usgs.gov/research/structure/crust/crust.php>). Stern and Johnson (2010) reviewed existing geophysical and petrologic studies and concluded that Arabian Plate continental crust was  $\sim 40$  km thick, commonly with a mid-crustal velocity step that is sometimes referred to as the “Conrad discontinuity”. Where found, the Conrad discontinuity occurs 15 to 20 km deep and separates lower  $V_p$  felsic upper crust from higher  $V_p$  mafic lower crust. Geophysical investigations of southern Jordan crust agree with this conclusion (Fig. 1C) (DESERT-Group, 2004). We want to sample the lower crust beneath this region to document it and compare it to global continental crust.

A second motivation for studying lower crustal xenoliths from NE Jordan is to probe the age of the crust beneath the northern Arabian Plate. There are no exposed basement rocks for ~700 km between the northernmost ANS in SW Jordan and the Bitlis Suture in SE Turkey (Fig. 1A). Crystalline basement beneath northern Saudi Arabia, Jordan, Syria, and Iraq is buried beneath thousands of meters of Phanerozoic sediments. Until recently it was assumed that the basement of this region was Neoproterozoic crust like that of the ANS, but results of two recent studies challenge this assumption: identification of ~1 Ga crust exposed on the edge of the ANS in Sinai (Be'eri-Shlevin et al., 2012) and a tract of Early Carboniferous crust inferred from ~357 Ma crustal xenoliths from Tel Thannoun in southern Syria (Stern et al., 2014). It is also widely accepted that Late Ediacaran–Early Paleozoic “Cadomian” crust (600–500 Ma), which makes the crust of SW Eurasia from Iberia to Iran, was derived from the northern margin of Gondwana (Garfunkel, 2015). It is possible that Cadomian crust might also underlie the buried interval, and if so, this would be a useful constraint and encourage future studies to define the nature of the ANS–Cadomian transition in northern Arabia. The region that we study sits near the middle of this buried interval, ~100 km SE of Tel Thannoun (Figs. 1A, 1B).

## 2. Geologic setting

Mafic and ultramafic xenoliths are abundant in lava fields (called harrats in Arabic) of Arabia south of the Bitlis Suture (Fig. 1A). Harrats formed in the last ~30 Ma and stretch discontinuously N–S for ~2500 km from Yemen to Turkey (Fig. 1A). Most Arabian xenoliths are found in alkali basalts that are younger than ~5 Ma (McGuire, 1988). An overview of what is known about Arabian peninsula mantle and lower crustal xenoliths can be found in Stern and Johnson (2010).

The largest harrat is Harrat As Shaam, which extends NW–SE for 500 km from northernmost Israel through southern Syria and eastern Jordan into northern Saudi Arabia (Fig. 1A). The crustal xenoliths that we studied are from two volcanoes in the Harrat As Shaam of NE Jordan, Abu Tarbush and Ashqaf Usefir. The xenoliths are hosted by Pliocene–Pleistocene lavas (4.52 to 1.0 Ma; Ilani et al., 2001) of the Ufayhim–Hashimyya basalt xenolithic formation of the Asfar Volcanic Group (Ibrahim et al., 2006). The 15–25 m thick Ufayhim Formation consists of olivine–phyric basanite to nepheline basanite and contains abundant (up to 25 xenoliths per sq. meter) mantle and crustal xenoliths (Ibrahim et al., 2006). Trace element modeling indicates that these magmas formed by low degree (2 to 5%) melting of garnet lherzolite asthenosphere (Shaw et al., 2003). Harrat As Shaam lavas erupted through Mesozoic and Paleozoic sediments. The nearest exposures of crystalline basement are found about 300 km away in SW Jordan: the ~900–610 Ma Aqaba Complex and the 605–550 Ma Araba Complex (Powell et al., 2015). The Araba Complex consists mostly of alluvial conglomerates and associated braided-river siliciclastic rocks, lavas and volcanoclastic deposits, along with dykes, granitoid stocks and minor monzogabbros and diorites, all with alkaline affinities and interpreted to have been emplaced in an extensional tectonic setting. Five boreholes (Fig. 1B) penetrated Phanerozoic sediments in northern Jordan and into Araba Complex basement, although none of these are situated as far NE as Abu Tarbush or Ashqaf Usefir.

## 3. Analytical techniques

We selected four xenoliths from Abu Tarbush (ABT) and five xenoliths from Ashqaf Usefir (AS) for study. Many xenoliths are ultramafic but we concentrated on crustal xenoliths for this study. The selected samples are large, some up to ca. 20 × 20 × 30 cm,

to yield enough material to be dated. We studied these crustal xenoliths using a range of analytical tools. These techniques are outlined briefly here and in detail in Supplementary Document 1. We used four main procedures: 1) petrographic microscope and electron microprobe (EPMA) to describe the petrography and determine mineral chemistry of the xenoliths (results in Supplementary Documents 2 and 3, as well as geothermometry using a range of techniques discussed in Supplementary Document 4 and results tabulated in Supplementary Document 5); 2) Inductively Coupled Plasma – Atomic Emission Spectroscopy, Inductively Coupled Plasma – Mass Spectrometry, and related techniques to determine whole-rock major and trace element chemical analyses (results in Supplementary Document 6); 3) Cathodoluminescence imaging of zircons (CL images in Supplementary Document 7); 4) ion microprobe analyses to determine U–Pb zircon ages (U–Th–Pb isotopic results in Supplementary Document 8); and 5) thermal ionization mass spectrometry to determine isotopic compositions of Sr, Nd, and Pb in whole rock samples (results in Supplementary Document 9). Sr, Nd, and Pb isotopic results were corrected for 560 Ma of radiogenic growth using the Rb, Sr, Sm, Nd, U, Th, and Pb concentrations in Supplementary Document 6. We studied 9 samples for petrography and using EPMA, 7 samples for whole-rock chemical composition, 4 samples for U–Pb zircon ages, and 7 samples for Sr, Nd, and Pb isotopes. The samples studied by the four different methods are summarized in Table 1.

## 4. Results

Below we present our results for petrographic, mineralogic, and mineral chemistry studies; whole-rock major and trace element chemical compositions; U–Pb zircon ages; and whole rock isotopic compositions of Sr, Nd, and Pb.

### 4.1. Petrography, mineralogy, and mineral chemistry

Detailed petrographic descriptions for the nine samples we studied using EPMA are provided in Supplementary Document 2 but a brief summary is provided here and in Table 1. The samples are mostly medium-grained, holocrystalline assemblages of plagioclase (Pl), orthopyroxene (Opx), and clinopyroxene (Cpx), sometimes with spinel (Sp; 2 ABT samples and 2 AS samples), more rarely with olivine (Ol; 2 ABT samples), pyrope-rich garnet (Grt; one AS sample) or pargasitic amphibole (Amp; 2 AS samples), along with oxide minerals (mostly ilmenite (Ilm) but also magnetite (Mag), sometimes altered to limonite (Lim)) as well as apatite (Ap). The samples have a granulitic appearance but we do not call them granulites because they are igneous rocks. Nevertheless, these rocks satisfy much of the IUGS definition of Coutinho et al. (2007) as a high-grade metamorphic rock in which Fe–Mg–silicates are dominantly hydroxyl-free, and that the presence of feldspar and the absence of primary muscovite are critical.

Our sample suite includes 3 gabbronorites, 4 norites, 1 gabbro, and a garnet clinopyroxenite. All samples contain abundant Pl and Opx (excepting spinel–garnet clinopyroxenite AS-23B). Ilmenite is the early-formed oxide phase. Norites contain much more orthopyroxene than clinopyroxene. These minerals we term “primary phases” to distinguish them from smaller grains forming microcrystalline “melt pockets” and reaction rims, especially of magnetite around ilmenite and clinopyroxene around orthopyroxene. Fig. 2 shows the petrography of the four samples that we dated (ABT5 and 6; AS 23 and 28). There is a hint of preferred orientation of grains but there is no well-defined mineral layering.

Primary phase compositions are summarized in Table 1 and Fig. 3. Some clinopyroxenes have Mg# ~90 (diopside) but most are augite. Orthopyroxenes mostly have Mg# between 50 and 80 and

**Table 1**  
Petrologic summary, Jordan lower crustal xenoliths.

| Volcano sample | Abu Tarbush                   |   |   |                                   | Ashaqef Usefir                          |  |   |                             |                                    |
|----------------|-------------------------------|---|---|-----------------------------------|---|--|---|-----------------------------|------------------------------------|
|                | ABT3                          | ABT5                                      | ABT6  | ABT8                              | AS9                                     | AS15                                     | AS23                                      | AS23B                       | AS 28                              |
| Lithology      | Norite                        | Norite                                    | Norite  | Gabbro                            | Gabbro                                  | Gabbro                                   | Norite                                    | Garnet Pyroxenite           | Gabbro                             |
| Mode           | PL50 CPX25 OPX18 SP5 LIM1 OL1 | PL68 OPX20 CPX1 AP7 ILM3 MT1              | PL70 OPX20 CPX1 AP4 ILM4 LIM1                 | PL35 CPX30 OPX20 ILM6 MT4 SP4 OL1 | PL30 CPX40 OPX5 AMPH2 SP1 ILM10 MT7 AP5 | PL55 OPX25 CPX20 ILM5 HEM1               | PL70 OPX20 CPX1 ILM4 LIM1 AP4             | CPX65 GRT25 SP9 Alteration1 | PL75 OPX12 CPX10 ILM2 HEM1         |
| Olivine        | FO 71–75                      |   |   | FO 62–71                          |   |  |   |                             |                                    |
| Spinel Cr#     | 0.001–0.003                   |   |   | 0.008–0.01                        | 0.0003–0.0013                           |  |   | 0.012–0.015                 |                                    |
| Clinopyroxene  | Wo48En38Fs10Ac4               | Wo45En35Fs19Ac1                           | Wo46En36Fs16Ac2                               | Wo47En37Fs13Ac3                   | Wo45En38Fs15Ac2                         | Wo48En37Fs12Ac3                          | Wo45En35Fs18Ac1.5                         | Wo50En41Fs4Ac5              | Wo47En39Fs11Ac3                    |
| Orthopyroxene  | Wo0.6En72Fs27                 | Wo1En55Fs44                               | Wo1En55Fs44                                   | Wo1En64Fs35                       | Wo1En65Fs34                             | Wo1En63Fs36                              | Wo1En55Fs44                               |                             | Wo1En75Fs26                        |
| Plagioclase    | An53–61                       | An42–54                                   | An44–48                                       | An56–61                           | An57–60                                 | An53–56                                  | An43–52                                   |                             | An65–81                            |
| Amphibole      |                               |   |   |                                   | Pargasite (4% TiO <sub>2</sub> )        |  |   |                             | Pargasite (3.5% TiO <sub>2</sub> ) |
| Garnet         |                               |   |   |                                   |   |  |   | Yes                         |                                    |
| Ilmenite       |                               |   |   |                                   |   |  |   |                             |                                    |
| Other minerals |                               |   |   |                                   |   |  |   |                             |                                    |
| Melt pockets   | 1%                            | TiO <sub>2</sub> 48% FeO 46% zeolite 1–2% | TiO <sub>2</sub> 50% FeO 46% Cpx hydrate 1–2% | TiO <sub>2</sub> 50% FeO 46%      | TiO <sub>2</sub> 30–50% + rutile 1%     | TiO <sub>2</sub> 43% or 53% zeolite none | TiO <sub>2</sub> 50% FeO 45% zeolite 2–3% |                             | TiO <sub>2</sub> 49–54% 10–12%     |
| Analyses       | 1                             | 1, 2, 3, 4                                | 1, 2, 3, 4                                    | 1, 2, 4                           | 1, 2, 4                                 | 1, 2, 4                                  | 1, 2, 3, 4                                | 1                           | 1, 2, 3, 4                         |

1: petrography and EPMA.

2: whole rock major and trace element geochemistry.

3: U–Pb zircon.

4: Sr–Nd–Pb isotopes.

are hypersthene. Feldspars are plagioclase mostly ranging in composition between An<sub>40</sub>Ab<sub>60</sub> and An<sub>60</sub>Ab<sub>40</sub> (andesine–labradorite) but with a few grains in AS samples as calcic as An<sub>84</sub>Ab<sub>16</sub> (bytownite). Spinel (ABT 3 and 8; AS 9 and 23B) are Al-rich with low Cr# (0.001 to 0.015) and Fe# ranging from 0.2 to 0.67. Olivine is only identified in AT 3 and 8 and is quite Fe-rich (Fo<sub>75</sub>Fa<sub>25</sub> to Fo<sub>62</sub>Fa<sub>38</sub>). No minerals expected for metasedimentary rocks such as aluminosilicates or carbonates were identified. The mineral compositions we observed in the xenoliths are those expected to form by slow crystallization of fractionated intermediate igneous rocks such as diorite and gabbro-diorite, and we conclude that these xenoliths are meta-igneous rocks.

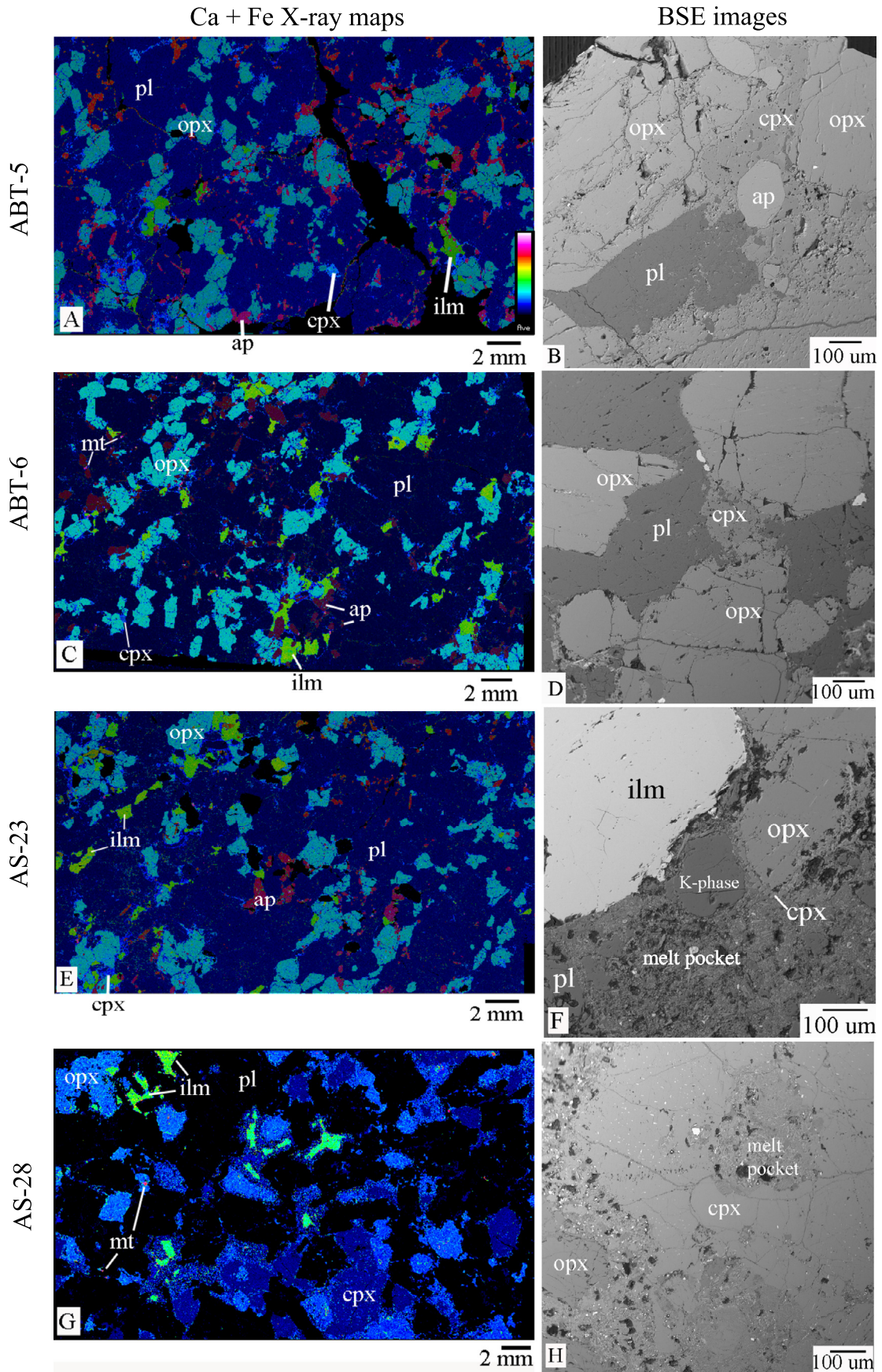
An important aspect of these xenoliths is the presence of segregations and infiltrations of microcrystalline “melt pockets”, mostly in interstices between primary phases (Fig. 2F). This seems to reflect a late infiltration of magma that was also responsible for corrosion and formation of thin rims around primary phases, especially of magnetite around ilmenite and clinopyroxene around orthopyroxene. Detailed study of the melt pockets and the K-rich phase is beyond the scope of this study but it is worth noting that these are broadly granitic and therefore unrelated to the host nepheline basalt/basanite.

We applied several mineral geothermometers in an effort to estimate equilibration temperatures for the xenoliths (Supplementary Documents 4 and 5). The most commonly used geothermometer for mafic and ultramafic rocks is based on element exchange reactions between mineral pairs, especially ortho- and clinopyroxene. These geothermometers are relatively insensitive to P. The approaches we used included those based on: 1) exchange of Fe and Mg between two pyroxenes (Brey and Köhler, 1990); 2) Ca contents in Opx (Brey and Köhler, 1990); 3) partitioning of Na between Opx and Cpx (Brey and Köhler, 1990); 4) multi-element partitioning between Cpx–Opx pairs (Putirka 2008); 5) reactions between different equilibrium mineral assemblages (Andersen et al., 1993); 6) Na in pyroxenes (Hervig and Smith, 1980); and 7) partitioning of Ca and Fe–Mg between garnet and Cpx. The P–T estimates are inconsistent, possibly reflecting the partial re-equilibration of the various primary minerals with the infiltrated melt. For instance, the first 6 geothermometers could be applied to most of the samples but the last could only be applied to garnet clinopyroxenite sample AS-23B. These several approaches gave T estimates ranging from 409 °C to 1293 °C, as summarized in Supplementary Documents 4 and 5. In the best case (AS15), T estimates ranged from 702 °C to 891 °C, which we consider too large of a range to be useful. The Putirka (2008) approach also provides P estimates, which range from 6 to 33.6 kbar. The samples we studied (with the possible exception of garnet clinopyroxenite sample AS-23B, which could be from the upper mantle) should be crustal in origin and the base of the crust should be at P ~ 13 kbar. Only 2 of the 9 samples give P estimates corresponding to the crust, so we consider these estimates to be unreliable. The approach of Andersen (1995) calculates oxygen fugacity (fO<sub>2</sub>) and this was determined for 5 samples; fO<sub>2</sub> ranged from –11.4 to –13.5, corresponding to –1.1 to +1.1 units around FMQ buffer.

#### 4.2. Whole-rock major and trace element chemistry

Whole-rock major and trace element geochemical data for 7 samples are listed in Supplementary Document 6, along with CIPW norms, Mg#, and selected trace element ratios. Fig. 4 summarizes compositional features of the Jordan xenoliths and compares them with lower crustal xenoliths from harrats in Arabia to the south and to Tel Thannoun, Syria, ~100 km to the NW (Fig. 1B).

The analyzed samples are ultramafic to mafic (37.4–50.8 wt.% SiO<sub>2</sub>; mean = 46 wt.%), manifested in a lack of normative quartz. One sample (AS-23) contains a small amount (3.6 wt.%) of nor-



native nepheline. We plot these results on classification diagrams to provide a geochemical overview. Because these rocks mostly are cumulates and not liquid compositions, these classifications must be regarded with caution. The xenoliths plot around the tholeiitic-calcalkaline divide on a plot of  $\text{FeO}^*/\text{MgO}$  vs.  $\text{SiO}_2$  (Fig. 4A). On a total alkalis–silica (TAS) classification diagram for plutonic rocks, the xenoliths plot in the gabbro field or below it (Fig. 4B). The xenoliths contain moderately high  $\text{Al}_2\text{O}_3$  (10.15–19.18 wt.%; mean =  $16.3 \pm 3.0$  wt.%), CaO (8.71–15.8 wt.%; mean =  $11.0 \pm 2.3$  wt.%) and  $\text{Na}_2\text{O}$  (0.87–3.81 wt.%; mean =  $2.5 \pm 0.9$  wt.%). This reflects abundant normative plagioclase (mean =  $48.0 \pm 13.8$  wt.%). None of the analyzed samples contain normative corundum, further indicating that they do not represent metamorphosed Al-rich pelites. The 7 samples show a tremendous range in  $\text{TiO}_2$  contents (0.1–6.32 wt.%; mean =  $1.7 \pm 2.0$  wt.%; Fig. 4C) and total iron as  $\text{Fe}_2\text{O}_3^T$  (6.34–21.9 wt.%; mean =  $10.9 \pm 4.7$  wt.%). This is partly reflected in significant and variable contents of normative ilmenite (mean =  $3.6 \pm 4.2$  wt.%) and magnetite (mean =  $2.5 \pm 1.1$  wt.%). Whole rock MgO contents vary 3 $\times$ , from 4.1 to 14.75 wt.% (mean =  $8.6 \pm 3.4$  wt.%), and this is reflected in large variations in Mg# (41 to 82). Analyzed xenoliths generally contain normative olivine (mean =  $13.7 \pm 10.6$  wt.%), diopside (mean =  $15.0 \pm 13.7$  wt.%), and hypersthene (mean =  $14.9 \pm 9.2$  wt.%). The xenoliths also contain widely variable  $\text{P}_2\text{O}_5$  (0.01–2.7 wt.%; mean =  $1.3 \pm 0.5$  wt.%; Fig. 3C) resulting in variable abundances of normative apatite =  $2.1 \pm 2.6$  wt.%. The xenoliths have low contents of  $\text{K}_2\text{O}$  and lie in the Low- and Medium-K fields on a  $\text{K}_2\text{O}$  vs.  $\text{SiO}_2$  plot (Fig. 4D). The xenoliths contain little C (mean =  $0.09 \pm 0.07$  wt.%) or S (mean =  $0.02 \pm 0.00$  wt.%) so the modest LOI (mean =  $1.3 \pm 0.5$  wt.%) must be water.

Three of the samples show major element compositions that are unusual for melts, for example  $\text{P}_2\text{O}_5$  enrichment in ABT5 and ABT6 and  $\text{TiO}_2$  enrichment in AS9. Such enrichments are common in cumulate igneous rocks. Similarly, the evolved nature of mineral compositions (e.g., Fe-rich pyroxene and olivine; intermediate plagioclase) contrasts with mafic whole rock major element composition and this also suggests that some of the samples we studied formed by crystal accumulation from an evolved melt.

Trace element and Rare Earth Element patterns are shown in Fig. 5, where they are also compared with a 585–600 Ma “A-type” granite from Feinan, Jordan (Fig. 1B). Trace element abundances in the xenoliths vary widely, as expected for cumulate igneous rocks. REE patterns show no significant difference between mafic and felsic samples. Abundances of compatible elements Cr and Ni range from 10 to 1320 ppm and 1 to 277 ppm, respectively; samples with high concentrations of these elements are probably cumulates. The xenoliths show strong enrichments in Ba, K, Sr, Pb, and Eu, elements sequestered in feldspars; samples with

positive Eu anomalies in Fig. 5 (ABT8, and AS28) are feldspar-rich cumulates. Unusual ratios of some incompatible trace elements are observed, for example K/Rb and K/U are unusually high (mean =  $1215 \pm 565$  and  $63000 \pm 60080$ , respectively) and Th/U is unusually low (mean =  $0.96 \pm 0.56$ ) compared to typical values for the bulk continental crust (K/Rb = 306; K/U = 11600; Th/U = 4.3; Rudnick and Gao, 2003). Similar features characterize other samples of lower crust (Rudnick, 1992).

#### 4.3. U–Pb zircon ages

Zircons were first imaged using cathodoluminescence (CL); examples of the CL images of Jordan lower crust xenoliths are provided in Supplementary Document 7. Fig. 6 shows the 4 U–Pb zircon ages obtained in this study, two norite xenoliths from Abu Tarbush and one each norite and gabbro-norite from Ashqaf Usefir. There are few zircons in these Zr-poor (<30 ppm) samples and these mostly have low U contents; nevertheless, the four samples give a very narrow and consistent range of ages:  $554 \pm 4$  Ma;  $559 \pm 5$  Ma;  $559 \pm 6$  Ma, and  $563 \pm 5$  Ma (Fig. 6). Further details are provided below.

##### 4.3.1. Abu Tarbush samples

4.3.1.1. Sample ABT-5 is a coarse-grained norite containing 23 ppm Zr. Zircon separated from it contain 9–66 ppm U, 5–70 ppm Th and Th/U = 0.62–1.3. We analyzed 15 zircon grains from this sample (Supplementary Document 8) and excluded six spot analyses from age calculation because these have high Th/U, show significantly

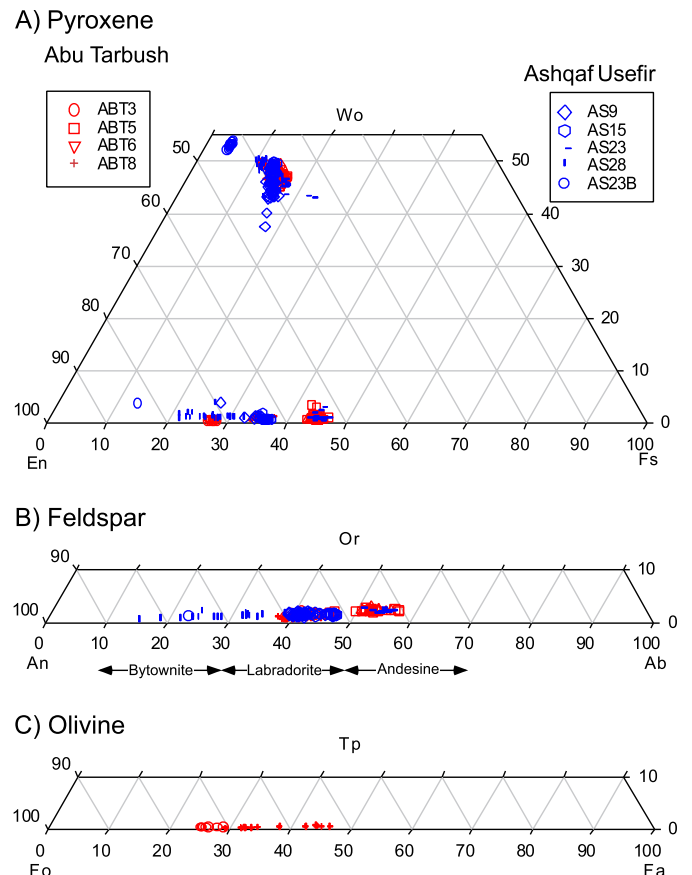


**Fig. 3.** Compositional summary of principal silicate minerals in lower crustal xenoliths from Abu Tarbush (red symbols) and Ashqaf Usefir (blue symbols): A) pyroxene (Wo = wollastonite, En = enstatite, Fs = ferrosilite); B) feldspar (An = anorthite, Ab = albite); and C) olivine (Fo = forsterite, Fa = fayalite). (For interpretation of the references to color in this figure legend, the reader is referred to the web version of this article.)

**Fig. 2.** Representative X-ray chemistry false-color maps showing the distribution of Ca and Fe (left panels) and back-scattered electron images (BSE, right) for the four Jordan xenolith samples from Abu Tarbush (ABT) and Ashqaf Usefir (AS) dated using U–Pb zircon techniques. A, B: ABT5 (norite): The image is 90% Opx and Pl, 10% Ap and Ilm, and ~1% Cpx and Mag. Opx, Pl and Cpx show disequilibrium textures. Most Opx have Fe–Ti oxide exsolution (forming thin white lamellae). Some grain boundaries show reaction/corrosion contacts. Color scale, from dark blue (low Ca + Fe, dark blue) to red and pink (high low Ca + Fe). C, D: ABT6 (norite): The image is 90% Opx and Pl, 10% Ap and Ilm, and ~1% Cpx and Mag. There are alterations along some Opx rims. Most Opx have Fe–Ti oxide exsolution. Melt pockets and defined by zones rich in Opx microcrystals around larger Pl. E, F: AS23 (norite): The image is ~90% Opx and Pl, ~10% Ap and Ilm, and ~1% Cpx and Lim. Most Opx have Fe–Ti oxide exsolution. BSE image shows microcrystalline “melt pockets” and reactions along grain boundaries. Note Cpx rims around Opx near contacts with Pl. G, H: AS28 (gabbro-norite): The image consists of 75% Pl, 13% Opx, and 10% Cpx, along with ~3% Ilm. BSE image shows microcrystalline “melt pockets” of Cpx, Pl, and Ilm along the contact between Opx and Cpx. The contacts show strong alteration and the contact zone contains Cpx, Pl, and Ilm microcrystals. (For interpretation of the references to color in this figure legend, the reader is referred to the web version of this article.)

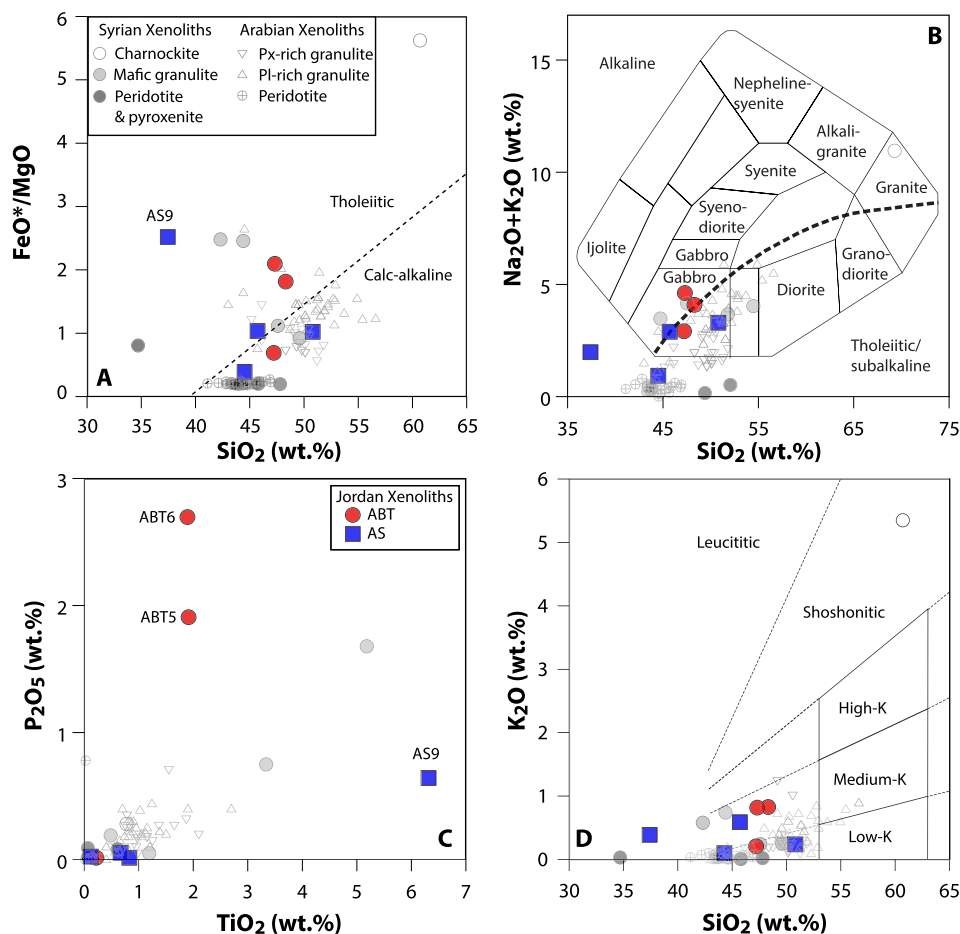


**Fig. 4.** Major element variations in crustal xenoliths from NE Jordan. Also shown for comparison are analyses for lower crust xenoliths (~357 Ma xenoliths from Tell Thannoun, Syria and lower crust and upper mantle xenoliths from Saudi Arabia (Stern et al., 2014)). A) wt.% FeO\*/MgO vs. SiO<sub>2</sub>; dashed line separates tholeiitic from calc-alkaline igneous rocks. B) Total alkalis – silica diagram for plutonic rocks (fields from Cox et al., 1979). C) wt.% P<sub>2</sub>O<sub>5</sub> vs. TiO<sub>2</sub>. D) wt.% K<sub>2</sub>O vs. SiO<sub>2</sub>.

lower <sup>206</sup>Pb/<sup>238</sup>U indicating Pb loss or are excessively discordant. The remaining nine analyses are concordant (Fig. 6a) and yield a concordia age of 563 ± 5 Ma (2σ, n = 9, MSWD = 1.3).

**4.3.1.2. Sample ABT-6** is a coarse-grained norite containing 24 ppm Zr. Zircon separated from this sample contains 13–88 ppm U, 10–50 ppm Th contents and Th/U from 0.5–1.1 (Supplementary Document 8). Out of twelve zircon grains analyzed (Fig. 1b), nine grains yield a concordia age of 559 ± 5 Ma (2σ, n = 9, MSWD = 1.8; Fig. 6b). Three analyses were excluded from age calculations because they yield much younger ages, probably due to Pb loss or a slightly younger metamorphic event, or are discordant.

#### 4.3.2. Ashqaf Usefir samples

**4.3.2.1. Sample AS-23** is a coarse-grained norite containing 8 ppm Zr. Zircon separated from this sample have 8–36 ppm U, 5–35 ppm Th and Th/U from 0.6–1.3 (Supplementary Document 8). One measurement was made on each of 7 grains and one grain (#3) was analyzed 3 times, for a total of 10 analyses. One analysis (spot 1) shows high uncertainty (<sup>207</sup>Pb/<sup>206</sup>Pb age = 487 ± 111 Ma) and a low <sup>206</sup>Pb/<sup>238</sup>U ratio indicative of Pb loss. The remaining nine analyses are concordant and yield a concordia age of 554 ± 4 Ma (95% confidence; MSWD = 2.1; Fig. 6c).

**4.3.2.2. Sample AS-28** is a coarse-grained gabbro-norite containing 29 ppm Zr. Zircons separated from it contains 116–407 ppm U, 52–318 ppm Th and Th/U from 0.5–1.0. We analyzed 9 zircon grains from this sample (Supplementary Document 8), one of

which (#6) was analyzed twice, for a total of 10 analyses. We excluded three spot analyses from age calculation because they have high common Pb, show significantly lower <sup>206</sup>Pb/<sup>238</sup>U ratios indicating Pb loss or a slightly younger metamorphic event or are discordant. One analysis (spot 10) shows reverse discordance, has high U content (361 ppm), and yields a much older <sup>206</sup>Pb/<sup>238</sup>U age (904 ± 16 Ma) compared to the other analyses. The remaining six analyses are concordant (Fig. 6d) and yield a concordia age of 559 ± 6 Ma (95% confidence, n = 6, MSWD = 2.3).

#### 4.4. Whole-rock isotopic compositions of Sr, Nd, and Pb

Isotopic compositions of Sr, Nd, and Pb are presented in Supplementary Document 9 and shown in Fig. 7. Rb/Sr ratios are low, so correcting for 560 Ma of radiogenic growth results in little change of <sup>87</sup>Sr/<sup>86</sup>Sr. Age-corrected <sup>87</sup>Sr/<sup>86</sup>Sr ranges from 0.70260 to 0.70352, which is a mantle-like signature. Initial Nd isotopic compositions (εNd<sub>560</sub>) range from +1.3 to +9.6; with the exception of unusually radiogenic garnet clinopyroxenite sample AS23B, (εNd<sub>560</sub>) ranges from +1.3 to +4.8 (mean = +3.3). With the exception of garnet clinopyroxenite AS23B, combined initial Sr and Nd isotopic compositions are similar to those of slightly older granitic rocks from Sinai (Figs. 7A, B), both showing strong affinities to Ediacaran moderately depleted mantle.

Initial Pb isotopic compositions fall on the <sup>207</sup>Pb/<sup>204</sup>Pb vs. <sup>206</sup>Pb/<sup>204</sup>Pb diagram between the growth curves for typical mantle and typical orogenic crust (orogene), similar to the field of juvenile arc terranes of Arabia. Two samples (ABT5 and 6) have distinctly

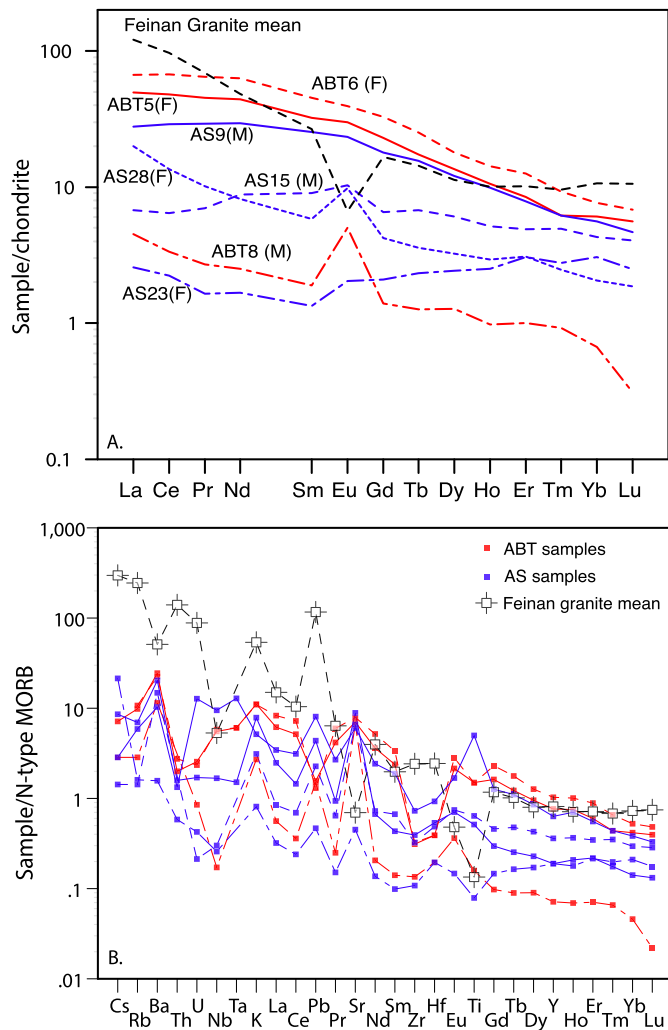


**Fig. 5.** A) chondrite-normalized Rare Earth Element patterns of Jordanian lower crust xenoliths. B) N-MORB normalized trace element patterns of Jordanian lower crust. Also shown for comparison is mean Feinan A-type granite from Jarrar et al. (2008). NE Jordan lower crust cumulates could be related to granites of similar age in the region.

higher initial  $^{207}\text{Pb}/^{204}\text{Pb}$  values and therefore may reflect greater involvement of subducted crustal material. In the  $^{208}\text{Pb}/^{204}\text{Pb}$  vs.  $^{206}\text{Pb}/^{204}\text{Pb}$  diagram, the data scatter, which is largely an artefact because for two samples (ABT8 and AS15) the Th contents were too low to be determined by ICP-MS and therefore, initial  $^{208}\text{Pb}/^{204}\text{Pb}$  could not be calculated directly, only constrained between the measured value and an initial  $^{208}\text{Pb}/^{204}\text{Pb}$  calculated assuming Th concentrations equivalent to the detection limit. Samples for which thorogenic Pb growth had been corrected fall between the field of juvenile arc terranes of Arabia and the orogenic crust. Three samples (ABT5 and 6, AS9) however, have markedly higher initial  $^{208}\text{Pb}/^{204}\text{Pb}$  values and fall in the compositional field of the Khida Paleoproterozoic terrane, indicating that this mantle source may have interacted with older crust. Note, because of the markedly higher Pb contents in crustal rocks than in mantle rocks, the Pb isotopic composition shows the crustal signature, whereas it is not apparent in the Sr and Nd isotopic composition.

## 5. Discussion

Below we discuss two questions about the lower crust beneath NE Jordan illuminated by our results; its composition and its age.

### 5.1. Nature and origin of lower crust beneath Northern Jordan

Geophysical and petrologic studies of Arabian peninsula crust consistently indicate that it is composed of upper felsic and lower mafic layers (Stern and Johnson, 2010). Our results are broadly consistent with this interpretation and extend the region where mafic lower crust can be identified into NE Jordan. Supplementary Document 6 presents an average composition (mean Jordan lower crust) for the xenoliths, which we take to approximate the lower crust composition beneath N. Jordan. N. Jordan mean lower crust is a plagioclase-rich 2-pyroxene igneous rock that is mafic ( $45.9 \pm 3.9$  wt.%  $\text{SiO}_2$ ) and fractionated ( $\text{Mg}\# \sim 61 \pm 14$ ).

We cannot constrain the P range at which the Abu Tarbush and Ashqaf Usefir xenoliths equilibrated, but these are mostly 2-pyroxene igneous rocks, which are thought to make up middle and lower continental crust (Bohlen and Mezger, 1989; Rudnick and Gao, 2003). Insofar as the xenoliths from two volcanoes that we have studied are representative, the lower crust beneath northern Jordan is a predominantly magmatic construction that formed over a brief interval from  $563 \pm 5$  Ma to  $554 \pm 4$  Ma. The wide range of chemical compositions and unusual enrichments of elements known to concentrate in distinctive phases indicate the presence of cumulate ilmenomagnetite and apatite found in some of the xenoliths is most easily explained if these are cumulate igneous rocks. We cannot relate these samples to fractionation of a single batch of mafic magma intruded into the lower crust, because of the wide range of initial isotopic compositions (although ABT5 and ABT6 could be from a single intrusive body). Fig. 8 illustrates the geologic processes we envision for formation of the crust of this region, combining our results with geophysical constraints on continental crustal structure (Christiansen and Mooney, 1995) and petrologic numerical models (Annen et al., 2006).

We cannot uniquely define the nature of the parental magma prior to fractionation in the lower crust, although this must have been broadly subalkaline basalt, because fractionation in some cases led to strong Fe-enrichment (Fig. 4A) and because samples plot in the low- and medium-K field on potash-silica diagram (Fig. 4D). Most samples show significant REE enrichment (Fig. 5), suggesting that the parental tholeiitic magma was enriched, although we cannot dismiss that some enrichment may reflect the effects of late K-rich melt infiltration.

It is not easy to infer the tectonic environment in which igneous activity happened. This is partly because cumulate igneous rocks are not suitable for interpretation using trace element-based tectonic discrimination diagrams designed for basalts. The results (intermediate magma, enrichments in Ba, K, Sr, Pb, and Eu, low Th/U, and Pb isotopic compositions) which generally suggest formation at a convergent plate margin, may be related to infiltrating high-K melt pockets. Similar K-feldspar veins and patches are known from other lower crust occurrences, where they are interpreted to reflect the inflow of low  $\text{H}_2\text{O}$ -activity brines derived from underplating mafic magmas in the lower crust (e.g., Franz and Harlov, 1998). The low  $\text{H}_2\text{O}$ -activity of the brine destabilized hydrated minerals like amphibole and biotite and modifies pyroxene chemistry at the same time that K-feldspar-rich segregations form. If the Jordan samples we analyzed did form at a convergent plate margin, the lack of strong SSZ-type enrichments typical of the magmatic front suggests formation in a reararc setting.

There is no hint in the samples that we studied about what if any crust existed in the region prior to the  $\sim 560$  Ma magmatic episode. The recognition of  $\sim 1$  Ga crust in Sinai (Be'eri-Shlevin et al., 2012) and of 357 Ma lower crust xenoliths from Tel Thannoun in S. Syria (Stern et al., 2014) suggests that crust beneath N. Jordan might also be of similar age, but there is no hint of such crust being present beneath N. Jordan. Initial isotopic compositions of Sr, Nd, and Pb are consistent with a mantle origin for the parental

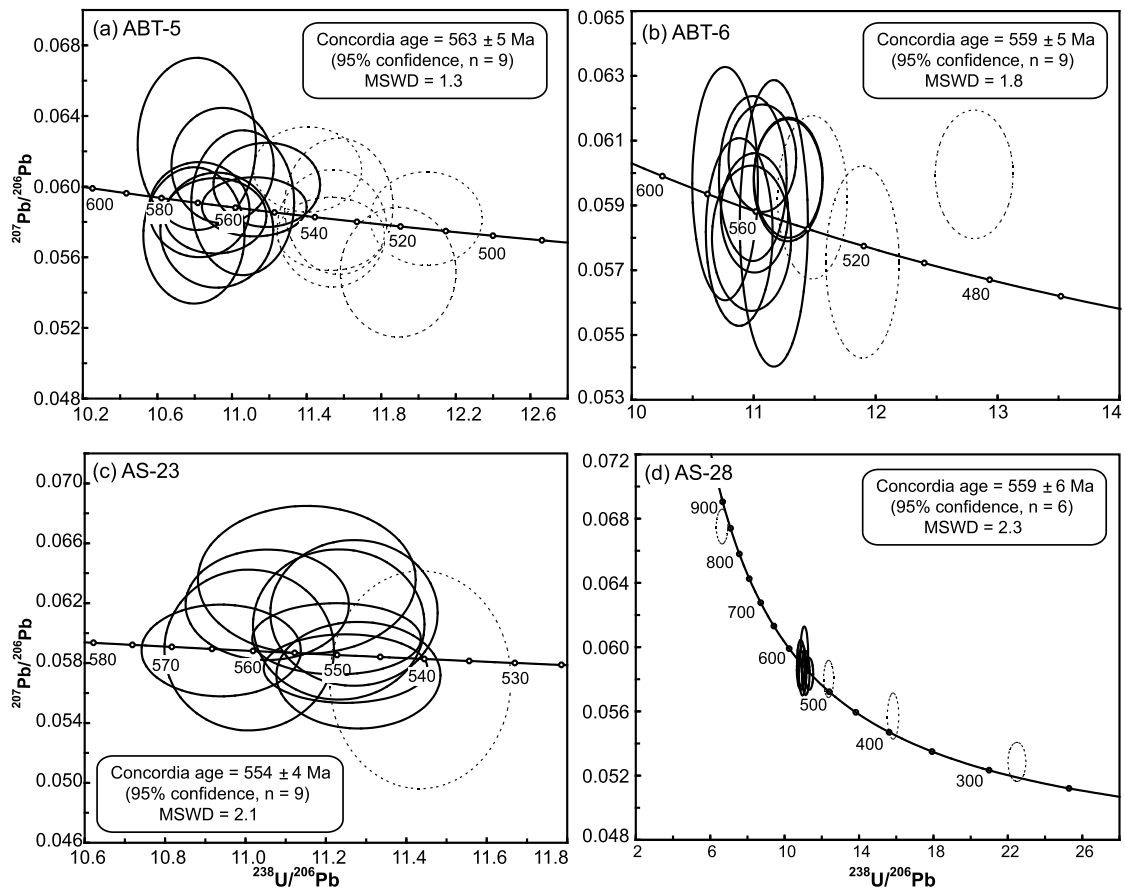


Fig. 6. U–Pb zircon ages for Jordan lower crustal xenoliths. See text for further discussion.

melts, with initial  $^{87}\text{Sr}/^{86}\text{Sr}$  ranging between 0.7026 and 0.7035, positive  $\varepsilon\text{Nd}_{(560)}$  (with the exception of a single, more radiogenic sample (+9.6), range = +1.3 to +4.8), initial Pb isotopic compositions that mostly plot between mantle and orogene (Fig. 7; Supplementary Document 9).

## 5.2. Age of crust beneath NE Jordan

The age range for the samples we dated ( $554 \pm 4$  Ma to  $563 \pm 5$  Ma) indicates a major magmatic episode beneath NE Jordan occurred at that time. This magmatic episode was significantly younger than the youngest igneous rocks of the Arabian–Nubian Shield to the south. The northernmost ANS in Egypt, Israel, Jordan and NW Saudi Arabia was intensely intruded by Ediacaran plutons and dikes and buried by volcanic rocks and associated debris. The northernmost ANS igneous record is best-documented for the granitic rocks of Sinai, where igneous activity evolved from early I-type to late A-type activity that peaked in intensity  $\sim 600$  Ma and ended by  $\sim 580$  Ma (Be’eri-Shlevin et al., 2009). Because northernmost ANS activity peaked  $\sim 40$  Myrs and ended  $\sim 20$  Myrs before formation of the crust beneath NE Jordan sampled by the xenoliths we studied, we conclude that this xenolith suite marks a younger magmatic episode than that forming the ANS. The simplest and most consistent explanation is that the crust beneath NE Jordan sampled by the xenoliths that we studied is a previously-unknown tract of Cadomian crust buried beneath the northern Arabian peninsula.

The Cadomian orogen reflects a Late Ediacaran to Early Cambrian peripheral accretionary margin and magmatic arc marking subduction beneath northern Gondwana (Fig. 9; Linnemann et al., 2010; Garfunkel, 2015). The Cadomian orogen was related to slightly older Neoproterozoic crust such as the ANS and its south-

ern extension, the East African Orogen, which formed earlier in the Neoproterozoic as interior orogens between colliding blocks of East and West Gondwana. Murphy and Nance (1991) proposed that as Gondwana amalgamated, the focus of subduction shifted from between the colliding blocks to around them (interior to peripheral), and the Avalonia–Cadmia arc is related to the latter stage. We do not know whether Cadomian crust beneath northern Arabia formed in place or was accreted. If it was accreted, this may have happened during the Late Ediacaran and Early Cambrian, before deposition of the undeformed Early Paleozoic platform succession (Powell et al., 2015) or during the Carboniferous “Hercynian” event, when large parts of N. Arabia were deformed (Konert et al., 2001).

During the time that Cadomia was attached to Gondwana  $\sim 560$ – $520$  Ma, the supercontinent Greater Gondwana reached its maximum size. This reconstruction of Greater Gondwana has many features in common with the alternative end-Precambrian reconstruction “Pannotia” (Dalziel, 1997), especially the core supercontinent of Gondwana. However, the two reconstructions differ in two important ways: 1) Pannotia shows N. America attached to western S. America, whereas Greater Gondwana does not, and 2) Greater Gondwana emphasizes Cadomian blocks on the northern flank. The arc, which originally probably extended from the northern margin of present South America along present northern Africa to Arabia and Iran, became fragmented and dispersed during the opening of the Rheic Ocean beginning as early as 520 Ma. Magmatic activity along the Cadomian arc was diachronous and possibly occurred in transpressional settings. In the eastern part of the Cadomian arc, subduction-related magmatism occurred at 620 to 540 Ma, followed by the intrusion of 540 to 520 Ma granitoids that reflect crustal heating, perhaps related to slab break-off (Linnemann et al., 2010).

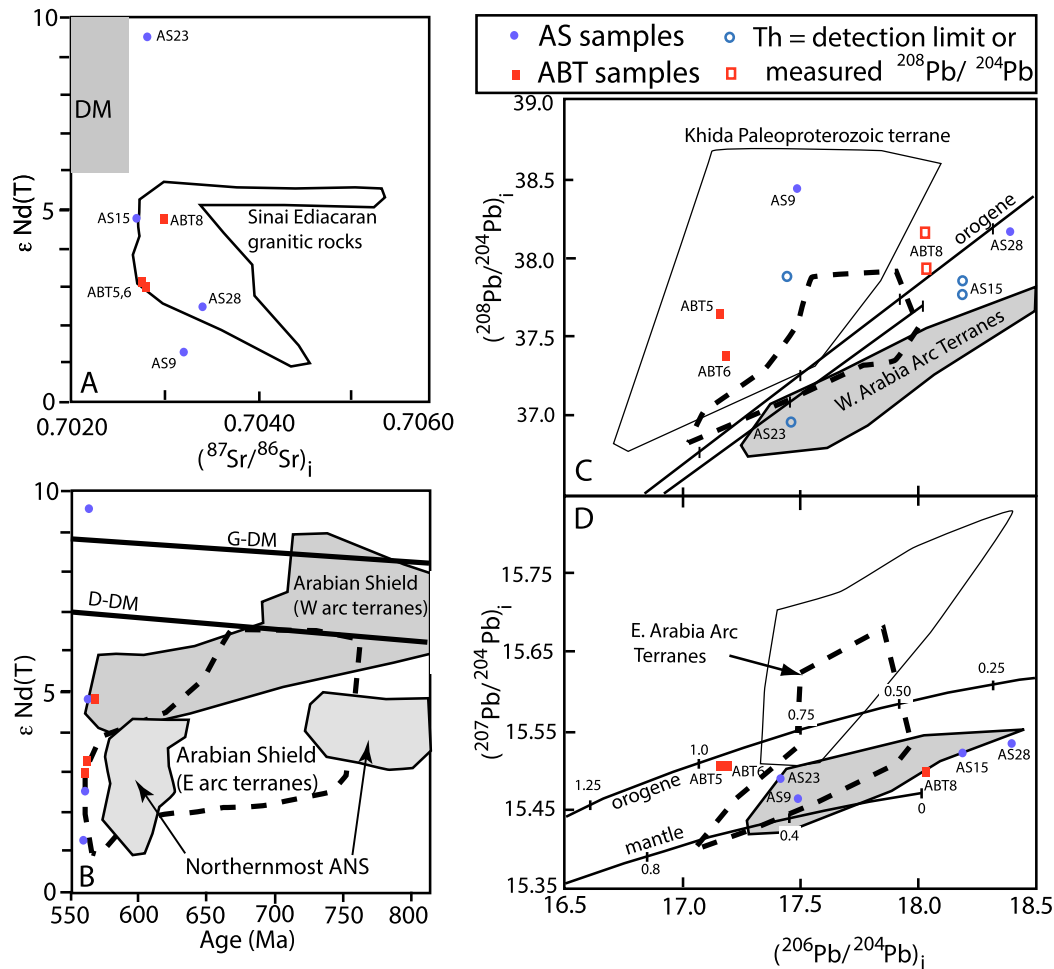


**Fig. 7.** Radiogenic isotopic compositions of Jordan whole-rock xenoliths, corrected for 560 Ma of radiogenic growth. Blue circles are for Ashqaf Usefir (AS) xenoliths and red boxes are for Abu Tarbush (ABT) xenoliths. A) Sr vs. Nd isotopes showing fields for 570–635 Ma granitic rocks of Sinai (Be’eri-Shlevin et al., 2010) and Depleted Mantle (DM). Note that with the exception of AS23 the samples have Sr- and Nd isotopic compositions like those of slightly older Sinai granitic rocks. B) Nd isotopic evolution diagram compared to depleted mantle evolution models of Goldstein et al (1984; G-DM) and DePaolo (1981; D-DM). Fields for Sinai granitic rocks after Be’eri-Shlevin et al. (2010). C)  $^{208}Pb/^{204}Pb$  vs.  $^{206}Pb/^{204}Pb$  corrected for 560 Ma radiogenic growth. Open symbols indicate three samples (ABT8, AS15, and AS23) that contain Th concentrations lower than ICP-MS detection limits; for each of these, two open symbols are shown: 1) measured  $^{208}Pb/^{204}Pb$ ; and 2) corrected for radiogenic growth using Th content = detection limit. Pb isotope fields and growth curves from Stoesser and Frost (2006).

The Cadomian magmatic arc later fragmented and separated from Gondwana, opening the Rheic Ocean; these fragments then accreted to the southern margin of Laurussia. Cadomian (and related Avalonian) fragments now form basement within the Paleozoic orogenic belts of eastern North America, southern Europe, Turkey, and Iran (Franke, 2000; Kroner and Romer, 2013).

Fragmentation of the Cadomian orogen and dispersal of its fragments left few known remnants attached to unaccreted Gondwana fragments of S. America, Africa, Arabia, Australia, and Antarctica (Karaoui et al., 2015; Thomas et al., 2015). It is not surprising that northern Arabia hides a tract of Cadomian crust, because Arabia projects farther north into the region than any other Gondwana fragment, into the region where Cadomian crust used to be. Our geochronologic results are most easily explained by a Cadomian crustal tract beneath the northern margin of the Arabian plate. NE Jordan is not the only place in the Arabian peninsula where evidence for Cadomian crust is found. Thomas et al. (2015) report U–Pb zircon ages of 546–560 Ma for four samples of volcanic rocks brought to the surface by three salt domes in the United Arab Emirates (Fig. 9) and similar ages were found for a volcanic clast brought to the surface by a salt dome in Oman. We note that these sites in NE Jordan and UAE–Oman are the first places on the relatively-intact remnants of Gondwana where Cadomian crust is identified. This recognition provides an important new constraint

for our understanding of the northern margin of Arabia. It is interesting to speculate that the younger parts of the Neoproterozoic Huqf Supergroup in Oman – the Ara Group and upper Nafun Groups – were strongly influenced by the Cadomian arc to the north, with initiation of the Cadomian arc marked by the development of the mid-Nafun (~600 Ma) unconformity. The Nafun–Ara boundary marks a shift from regional subsidence to a tectonic style characterized by uplift of large basement blocks which segmented the broader basin into several fault-bounded sub-basins (Immerz et al., 2000). Latest Ediacaran (~541–547 Ma) volcanic rocks in the northern Ara Group (Bowring et al., 2007) in particular may reflect distal (rear-arc) volcanic activity behind the Cadomian arc.

## 6. Conclusions

We studied nine lower crustal xenoliths brought to the surface in Neogene time by two volcanoes in Harrat As Shaam, NE Jordan. Using petrological, geochemical and isotopic analyses and U–Pb zircon dating, we have shown that the lower continental crust beneath this region formed during the latest Neoproterozoic, around 560 Ma. Most of the studied xenoliths are plagioclase-rich, 2-pyroxene igneous rocks with ilmenite and magnetite and one is a garnet clinopyroxenite. Geochemical and isotopic data suggest that these xenoliths formed by crystal accumulation from a fractionated, enriched tholeiitic magma emplaced deep in the crust. Sr and

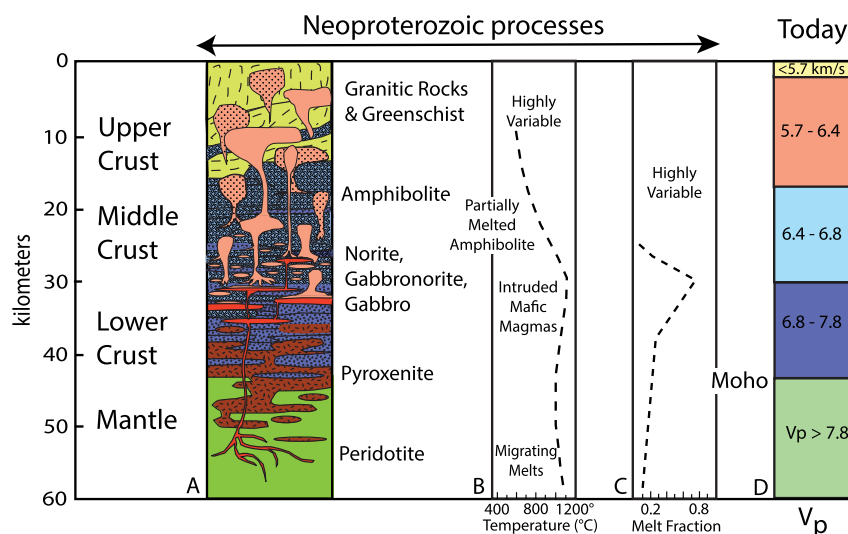


**Fig. 8.** Sections through the crust and upper mantle beneath Arabia. A) Generalized lithologic structure of Arabian crust and upper mantle as it might have existed in Late Ediacaran time. Solidified igneous rocks are patterned, partially molten zones are unpatterned (red = mafic, flesh = felsic). B) Modeled temperature variations as a function of depth 3.2 Myr after initiating “hot zone”, comprising basaltic sills injected into the lower crust (Annen et al., 2006). Sills 50 m thick are injected every 10 kyr, i.e. at an average emplacement rate of 5 mm/yr, see Annen et al. (2006) for further details. C) Variation of melt fraction as a function of depth, taken as a snapshot 3.2 Myr after initiating the hot zone, see Annen et al. (2006) for further details. D) Average P-wave velocity structure (km/sec) for Shields and Platforms (Christensen and Mooney, 1995), similar to the crustal structure beneath the Arabian Shield and the study area. (For interpretation of the references to color in this figure legend, the reader is referred to the web version of this article.)

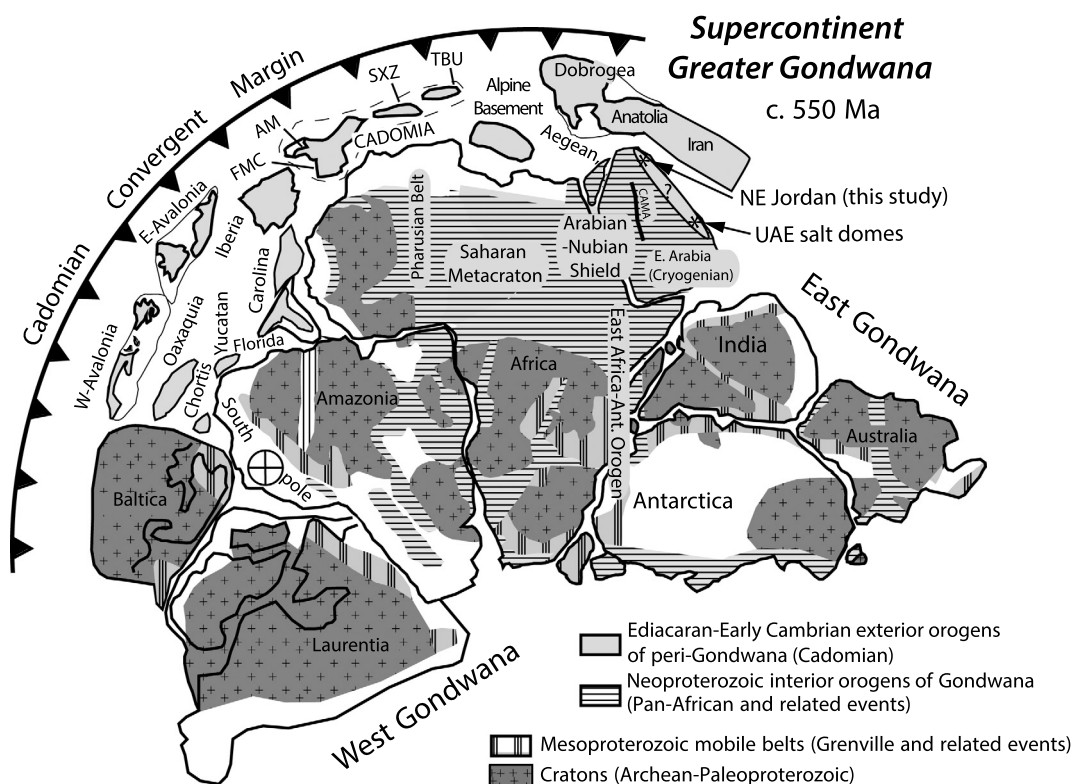


**Fig. 9.** Palaeogeography of the Cadomian – Avalonian active margin and related major peri-Gondwanan terranes at ~550 Ma (modified after Linnemann et al., 2010). AM Armorian Massif, FMC French Massif Central, SXZ Saxo-Thuringian Zone (part of the Bohemian Massif), TBU Teplá-Barrandian Unit (part of the Bohemian Massif). Location of the Central Arabian Magnetic Anomaly (CAMA) separating Cryogenian–Ediacaran crust of the Arabian–Nubian Shield from Cryogenian crust of E. Arabia is from Stern and Johnson (2010). It is not surprising that northern Arabia hides a tract of Cadomian crust, because Arabia projects farther north into the region than most other Gondwana fragments, into the region where Cadomian crust used to be. Location of salt domes bringing fragments of Cadomian rocks to the surface (UAE salt domes) is from Thomas et al. (2015).

Nd isotopic compositions indicate that the parental magmas were melts of depleted mantle, most likely in a reararc tectonic setting. Because magmatic activity in the Arabian–Nubian Shield peaked ~40 Myrs and ended ~20 Myrs before formation of the crust beneath NE Jordan, we conclude that the xenolith suite marks a different magmatic episode than that responsible for forming the

ANS, most likely as part of the Cadomian convergent margin, along the northern perimeter of the Greater Gondwana supercontinent. Recent results including ours indicate that the buried crust of N. Arabia is a complex amalgamation of arcs and rifts, not a simple continuation of the Cryogenian–Ediacaran Arabian–Nubian Shield. Crust buried beneath the northern Arabian peninsula is likely to

include older crust, likely including material similar to Grenville-aged crust of Sinai as well as younger crust, such as Cadomian documented for NE Jordan and UAE and Carboniferous crust of S. Syria. We clearly have much to learn about the buried crust of this region. It is still unknown how the transition from earlier E-W “Pan-African” convergence to the slightly younger peripheral Cadomian regime was accomplished, but evidence of this transition is likely preserved beneath the sediments of Jordan. Advancing our understanding of this transition could be accomplished by studying samples of the basement recovered by drilling (Fig. 1B) and integrating these results with compiled potential field (magnetic and gravity) data for the region.

### Acknowledgements

Thanks to the University of Jordan, Amman for logistic support during fieldwork. Thanks to William Bajjali and Mustafa Al Kuisi for generating the Jordan geologic map (Fig. 1B). We are grateful for careful reviews by J. Brendan Murphy and Marina Koreshkova. This is publication # 434 of the Nordic ion microprobe facility (Nordsim).

### Appendix A. Supplementary material

Supplementary material related to this article can be found online at <http://dx.doi.org/10.1016/j.epsl.2015.12.026>.

### References

- Abdelsalam, M.G., Stern, R.J., 1997. Sutures and shear zones in the Arabian–Nubian Shield. *J. Afr. Earth Sci.* 23, 289–310.
- Andersen, D.J., Lindsley, D., Davidson, P.M., 1993. QUILF: a PASCAL program to assess equilibria among Fe–Mg–Mn–Ti oxides, pyroxenes, olivine, and quartz. *Comput. Geosci.* 19, 1333–1350.
- Annen, C., Blundy, J.D., Sparks, R.S.J., 2006. The genesis of Intermediate and silicic magmas in deep crustal hot zones. *J. Petrol.* 47, 505–539.
- Avigad, D., Gvirtzman, Z., 2009. Late Neoproterozoic rise and fall of the northern Arabian–Nubian Shield: the role of lithospheric mantle delamination and subsequent thermal subsidence. *Tectonophysics* 477, 217–228.
- Be’eri-Shlevin, Y., Katzir, Y., Whitehouse, M.J., 2009. Post-collisional tectono-magmatic evolution in the northern Arabian Nubian Shield (ANS): time constraints from ion-probe U–Pb dating of zircon. *J. Geol. Soc. Lond.* 166, 71–85.
- Be’eri-Shlevin, Y., Eyal, M., Eyal, Y., Whitehouse, M.J., Litvinovsky, B., 2012. The Sa’al volcano-sedimentary complex (Sinai, Egypt): a latest Mesoproterozoic volcanic arc in the northern Arabian Nubian Shield. *Geology* 40, 403–406.
- Be’eri-Shlevin, Y., Katzir, Y., Blichert-Toft, J., Kleinhans, I.C., Whitehouse, M.J., 2010. Nd–Sr–Hf–O isotope provinciality in the northernmost Arabian–Nubian Shield: implications for crustal evolution. *Contrib. Mineral. Petrol.* 160, 181–201.
- Bohlen, S.R., Mezger, K., 1989. Origin of granulite terranes and the formation of the lowermost continental crust. *Science* 244, 326–329.
- Bowring, S.A., Grotzinger, J.P., Condon, D.J., Ramezani, J., Newhall, M.J., Allen, P.A., 2007. Geochronologic constraints on the chronostratigraphic framework of the Neoproterozoic Huqf supergroup, Sultanate of Oman. *Am. J. Sci.* 307, 1097–1145.
- Brey, G.P., Köhler, T., 1990. Geothermobarometry in 4-phase lherzolites II. New thermobarometers and practical assessment of existing thermobarometers. *J. Petrol.* 31, 1353–1378.
- Christiansen, N.I., Mooney, W.D., 1995. Seismic velocity structure and composition of the continental crust. *J. Geophys. Res., Solid Earth* 100, 9761–9788.
- Coutinho, J., Krätner, H., Sassi, F., Schmid, R., Sen, S., 2007. Amphibolite and granulite. In: Fettes, D., Desmons, J. (Eds.), *Metamorphic Rocks – A Classification and Glossary of Terms*. Cambridge University Press, pp. 51–57.
- Cox, K.G., Bell, J.D., Pankhurst, R.J., 1979. *The Interpretation of Igneous Rocks*. George Allen & Unwin, 450 p.
- Dalziel, I.W.D., 1997. Neoproterozoic–Paleozoic geography and tectonics: review, hypothesis and environmental speculation. *Bull. Geol. Soc. Am.* 109, 16–42.
- DePaolo, D.J., 1981. Neodymium isotopes in the Colorado Front Range and crust mantle evolution in the Proterozoic. *Nature* 291, 193–196.
- DESERT-Group, 2004. The crustal structure of the Dead Sea Transform. *Geophys. J. Int.* 156, 655–681.
- Franke, W., 2000. The mid-European segment of the Variscides: tectonostratigraphic units, terrane boundaries and plate tectonic evolution. In: Franke, W., Haak, V., Oncken, O., Tanner, D. (Eds.), *Orogenic Processes: Quantification and Modelling in the Variscan Belt*. In: *Spec. Publ.*, vol. 179. Geol. Soc., London, pp. 35–61.
- Franz, L., Harlov, D., 1998. High grade K-feldspar veining in granulites from the Ivrea-Verbano zone, northern Italy: fluid flow in the lower crust and implications for granulite facies genesis. *J. Geol.* 106, 455–472.
- Fritz, H., Abdelsalam, M., Ali, K., Bingen, B., Collins, A.S., Fowler, A.R., Ghebreab, W., Hauzenberger, C.A., Johnson, P., Kusky, T., Macey, P., Muhongo, S., Stern, R.J., Viola, G., 2013. Orogen styles in the East African Orogens: a review of the Neoproterozoic to Cambrian tectonic evolution. *J. Afr. Earth Sci.* 86, 65–106.
- Garfunkel, Z., 2015. The relations between Gondwana and the adjacent peripheral Cadomian domain – constraints on the origin, history, and paleogeography of the peripheral domain. *Gondwana Res.* 28, 1257–1281.
- Goldstein, S.L., O’Nions, R.K., Hamilton, P.J., 1984. A Sm–Nd isotopic study of atmospheric dusts and particulates from major river systems. *Earth Planet. Sci. Lett.* 70, 221–236.
- Hargrove, U.S., Stern, R.J., Kimura, J.-I., Manton, W.I., Johnson, P.R., 2006. How juvenile is the Arabian–Nubian Shield? Evidence from Nd isotopes and pre-Neoproterozoic inherited zircon in the Bi’r Umq suture zone, Saudi Arabia. *Earth Planet. Sci. Lett.* 252, 308–326.
- Hervig, R.L., Smith, J.V., 1980. Sodium thermometer for pyroxenes in garnet and spinel lherzolites. *J. Petrol.* 88, 337–342.
- Ibrahim, K.M., Shaw, J., Baker, J., Khoury, H., Rabba, I., Tarawneh, K., 2006. Pliocene–Pleistocene volcanism in north-western Arabian Plate (Jordan). I. Geology and geochemistry of the Asfar Volcanic Group. *N. Jb. Geol. Palaeont. Abh.* 242, 145–170.
- Ilani, S., Harlavan, Y., Tarawneh, K., Rabba, I., Weinberger, R., Ibrahim, K., Peltz, S., Steinitz, G., 2001. New K–Ar ages of basalts from the Harrat Ash Shaam volcanic field in Jordan: implications for the span and duration of the upper mantle upwelling beneath the western Arabian plate. *Geology* 29, 171–174.
- Immerz, P., Oterdoom, W.H., El Tonbary, M., 2000. The Huqf/Haima hydrocarbon system of Oman and the terminal phase of the Pan-African Orogeny; evaporite deposition in a compressive setting. *GeoArabia (Manama)* 5, 113–114.
- Jarrar, G.H., Manton, W.I., Stern, R.J., Zachmann, D., 2008. Late Neoproterozoic A-type granites in the northernmost Arabian–Nubian Shield formed by fractionation of basaltic melts. *Chem. Erde* 68, 295–312.
- Karaoui, B., Breitzkreuz, C., Mahmoudi, A., Youbi, N., Hofmann, M., Gärtner, A., Linne-mann, U., 2015. U–Pb zircon ages from volcanic and sedimentary rocks of the Ediacaran Bas Draa inlie (Anti-Atlas Morocco): chronostratigraphic and provenance implications. *Precambrian Res.* 263, 43–58.
- Konert, G., Affi, A.M., Al-Harjri, S.A., Droste, H.J., 2001. Paleozoic stratigraphic and hydrocarbon habitat of the Arabian Plate. *GeoArabia* 6, 407–442.
- Kroner, U., Romer, R.L., 2013. Two plates—many subduction zones: the Variscan orogeny reconsidered. *Gondwana Res.* 24, 298–329.
- Linnemann, U., Romer, R.L., Gerdes, A., Jeffries, T.E., Drost, K., Ulrich, J., 2010. The Cadomian orogeny in the Saxo-Thuringian zone. In: Linnemann, U., Romer, R.L. (Eds.), *Pre-Mesozoic Geology of Saxo-Thuringia – From the Cadomian Active Margin to the Variscan Orogen*. Schweizerbart, Stuttgart, pp. 37–58.
- McGuire, A.V., 1988. The mantle beneath the Red Sea: xenoliths from western Saudi Arabia. *Tectonophysics* 150, 101–119.
- Meyer, S.E., Passchier, C., Abu-Alam, T., Stüwe, K., 2014. A strike-slip core complex from the Najd fault system, Arabian shield. *Terra Nova* 26, 387–394.
- Mohsen, A., Kind, R., Sobolev, S.V., Weber, M., DESERT-Group, 2006. Thickness of the lithosphere east of the Dead Sea Transform. *Geophys. J. Int.* 167, 845–852.
- Mooney, W.D., Laske, G., Masters, T.G., 1998. CRUST 5.1: a global crustal model at 5° × 5°. *J. Geophys. Res.* B 103, 727–747.
- Murphy, J.B., Nance, R.D., 1991. Supercontinent model for the contrasting character of Late Proterozoic orogenic belts. *Geology* 19, 469–472.
- Powell, J.H., Abed, A., Jarrar, G.H., 2015. Ediacaran Araba Complex of Jordan. *GeoArabia* 20, 99–156.
- Putirka, K.D., 2008. Thermometers and barometers for volcanic systems. In: Putirka, K.D., Tepley, F.J. (Eds.), *Minerals, Inclusions and Volcanic Processes*. In: *Reviews in Mineralogy and Geochemistry*, vol. 69, pp. 61–120.
- Robinson, F.A., Foden, J.D., Collins, A.S., 2015. Geochemical and isotopic constraints on island arc, synorogenic, post-orogenic and anorogenic granitoids in the Arabian Shield, Saudi Arabia. *Lithos* 220–223, 97–115.
- Rudnick, R.L., 1992. Restites, Eu anomalies, and the lower continental crust. *Geochim. Cosmochim. Acta* 56, 963–970.
- Rudnick, R.L., Gao, S., 2003. The composition of the continental crust. In: Rudnick, R.L. (Ed.), *The Crust*, vol. 3. Elsevier, Amsterdam, pp. 1–64.
- Shaw, J., Baker, J., Menzies, M., Thirwall, M., Ibrahim, K.M., 2003. Petrogenesis of largest intraplate volcanic field on the Arabian plate (Jordan): a mixed lithosphere–asthenosphere source activated by lithospheric extension. *J. Petrol.* 44, 1657–1679.
- Stern, R.J., Johnson, P., 2010. Continental lithosphere of the Arabian Plate: a geologic, petrologic, and geophysical synthesis. *Earth–Sci. Rev.* 101, 29–67.
- Stern, R.J., Ren, M., Ali, K., Förster, H.-J., Al Safarjalani, A., Nasir, S., Whitehouse, M.J., Leybourne, M.I., 2014. Early Carboniferous (~357 Ma) crust beneath northern Arabia: tales from Tel Thannoun (southern Syria). *Earth Planet. Sci. Lett.* 393, 83–93.
- Stoeser, D.B., Frost, C.D., 2006. Nd, Pb, Sr, and O isotopic characterization of Saudi Arabian shield terranes. *Chem. Geol.* 226, 163–188.
- Thomas, R.J., Ellison, R.A., Goodenough, K.M., Roberts, N.M.W., All, P.A., 2015. Salt domes of the UAE and Oman: probing eastern Arabia. *Precambrian Res.* 256, 1–16.